ChemComm

COMMUNICATION

View Article Online
View Journal | View Issue

Open Access Article. Published on 05 novembris 2025. Downloaded on 10.01.2026 17:50:41.
This article is licensed under a Creative Commons Attribution-NonCommercial 3.0 Unported Licence.

Check for updates

Cite this: *Chem. Commun.*, 2025, **61**, 19237

Received 18th August 2025,
Accepted 30th October 2025

DOI: 10.1039/d5cc04768d

rsc.li/chemcomm

Cyclometallated iridium(III) complexes: ligand-driven selectivity for chemotherapy and photodynamic therapy

Eva Morales-Pioz,[a] Marta Redrado,[b] Andrea Benedi,[a] Araceli de Aquino,[c] Pilar García-Orduña,[a] María Royo-Cañas,[d] Javier Godino,[e] I. Marzo,[f] Laura Rodríguez,[c] M. Concepción Gimeno *[a] and Vanesa Fernández-Moreira *[a]

This study explores two cyclometallated Ir(III) complex families with distinct therapeutic profiles. Benzothiophene derivatives (1, 2) exhibit potent antiproliferative character in the dark, favoring chemotherapy, while benzothiazole analogs (3 and 4) show high photocytotoxicity, ideal for photodynamic therapy. Photophysical studies and subcellular localization analyses highlight ligand-driven selectivity and the role of organelle targeting in therapeutic outcomes.

Chemotherapy and photodynamic therapy (PDT) are key cancer treatments where metallodrugs have shown great potential. Since cisplatin's anticancer properties discovery in 1965, several Pt(II), Ru(II), Au(I), As(I), and Fe(II) compounds have reached clinical use.[1] Improving selectivity and potency remains central, often through rational ligand design. Although PDT's clinical adoption was initially limited by technology, recent advances like TOOKAD® (Pd(II) porphyrin) and TLD1433 (Ru(II) complex)[2] have promoted the interest in metal-based photosensitizers.[3,4] Traditional tetrapyrrolic photosensitizers face limitations in solubility, stability, and synthetic accessibility, whereas d^6 metal complexes, particularly Ir(III) compounds, offer tunable photophysical properties, efficient singlet oxygen generation, and deep tissue penetration, making them promising candidates for PDT applications.[5,6] For example, Gasser and Chao reported mitochondrial-targeting Ir(III) photosensitizers that induce immunogenic cell death,[7] while Brabec[8] and Mao[9] described complexes targeting mitochondrial DNA or damaging lysosomes, respectively. Additionally, Espino and Massager developed β-carboline-based Ir(III) photosensitizers with high selectivity against prostate cancer cells.[10]

Despite recent advances, achieving predictable therapeutic selectivity remains challenging due to the complexity of the tumor microenvironment, including oxidative stress, pH, and cellular heterogeneity.[11] In fact we previously reported pyrazole-based Ir(III) complexes showing cell-line-dependent activity as both chemotherapeutic agents and photosensitizers, highlighting the need for deeper mechanistic understanding.[12] To further explore how ligand design influences therapeutic outcomes, we investigated $[Ir(C^N)_2(N^N)]^+$ complexes bearing either 2-pyridylbenzothiophene (Py-Btp) or 2-phenylbenzothiazole (Ph-Btz) as C^N ligands (Fig. 1), chosen for their oxygen-sensitive emission and promising PDT potential.[13,14] In this study, we evaluate their performance in combination with benzimidazole-based N^N ligands for selective chemotherapy and PDT. Complexes **1–4** were synthesized as shown in Fig. S1 and fully characterized by ^{1}H and ^{13}C NMR (including COSY, HSQC, and HMBC), HRMS, and elemental analysis (Fig. S2–S27). Additional X-ray diffraction of complex **3** supports the given octahedral connectivity, Fig. 2a, Fig. S28 and Table S1.

Complexes **1–4** exhibited characteristic absorption features, with intense LC ($\pi \rightarrow \pi^*$) bands between 293–350 nm ($\varepsilon \approx 33\,000$–$40\,000$ M^{-1} cm^{-1}) and weaker MLCT bands in the 400–464 nm

[a] Instituto de Síntesis Química y Catálisis Homogénea (ISQCH), CSIC-Universidad de Zaragoza, Pedro Cerbuna 12, 50009 Zaragoza, Spain. E-mail: gimeno@unizar.es, vanesa@unizar.es
[b] Chimie ParisTech, PSL University, CNRS, Institute of Chemistry for Life and Health Sciences, Laboratory for Inorganic Chemical Biology, 75005 Paris, France
[c] Departament de Química Inorgànica i Orgànica, Secció de Química Inorgànica, Universitat de Barcelona, Martí i Franquès 1-11, 08028 Barcelona, Spain
[d] Servicio Científico-Técnico de Microscopía e Imagen, Instituto Aragonés de Ciencias de la Salud, 50009 Zaragoza, Spain
[e] Servicio Científico-Técnico de Separación Celular y Citometría, Instituto Aragonés de Ciencias de la Salud, 50009 Zaragoza, Spain
[f] Departamento de Bioquímica y Biología Molecular, Universidad de Zaragoza, 50009 Zaragoza, Spain

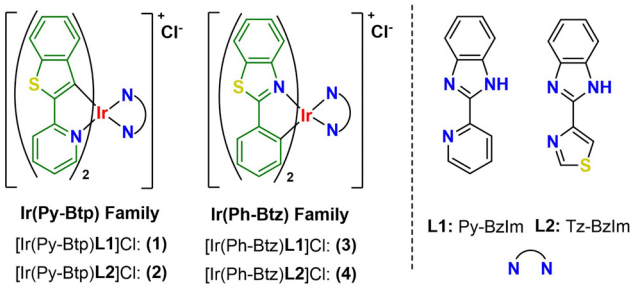

Fig. 1 Structures of complexes **1–4**.

Open Access Article. Published on 05 novembris 2025. Downloaded on 10.01.2026 17:50:41.
This article is licensed under a Creative Commons Attribution-NonCommercial 3.0 Unported Licence.

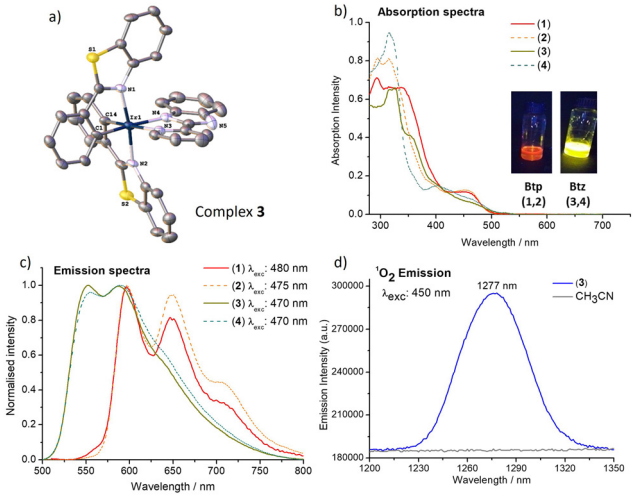

Fig. 2 (a) Crystal structure of cationic complex **3** (H atoms omitted for clarity). (b) Absorption and (c) emission spectra of **1–4** in DMSO (5×10^{-5} M). (d) Singlet oxygen generation by **3** in CH_3CN (5×10^{-5} M) upon 450 nm excitation.

range (Fig. 2b).[15] The absorption tails beyond 500 nm suggest contributions from triplet MLCT and/or LC states. UV-vis spectra after 48 h in DMSO and PBS : DMSO (9 : 1) confirmed good stability (Fig. S30–S33). Upon irradiation, all complexes showed phosphorescence in fluid solution (DMSO and CH_3CN) at 298 K (Fig. S34–S43), with emission spectra presented in Fig. 2c and S44–S47 and summarized in Table 1 and Table S2. Structured emission was observed for benzothiophene-based complexes **1** and **2** (λ_{em} = 595–598 nm, with tails >750 nm), consistent with a ^{3}LC (C^N, $\pi \rightarrow \pi^*$) character.[16] In contrast, benzothiazole analogues **3** and **4** emitted near 570 nm with unstructured profiles, indicative of enhanced MLCT ($d\pi$(Ir) $\rightarrow \pi^*$(N^N)) / LLCT (π(C^N) $\rightarrow \pi^*$(N^N)) mixing.[17] In aerated solution emission lifetimes were shorter in CH_3CN than in DMSO due to oxygen quenching (Fig. S34–S43). Accordingly, quantum yields increased in deoxygenated DMSO, reaching 38% (**1** and **2**), and 83% (**3** and **4**).

Singlet oxygen generation was confirmed by emission at 1272 nm under 450 nm excitation in aerated CH_3CN (Fig. 2d and Fig. S48–S50), with no signal in neat solvent, excluding artefacts. Using perinaphthenone as a reference, $^1O_2$ quantum yields ranged from 44–55%, highlighting the strong photosensitizing potential of all complexes for PDT.

The antiproliferative activity of Ir(III) complexes **1–4** was analysed in A549 (lung) and HeLa (cervical) cancer cells, in the dark and under irradiation, Table 2. Upon light exposure, all complexes exhibited enhanced antiproliferative effect, probably related to $^1O_2$ generation. In A549 cells, light-activated IC_{50} values were $\leq$0.34 μM. In the dark, Btp complexes **1** and **2** were active ($IC_{50} \approx 1$ μM), while Btz analogues **3** and **4** were far less ($IC_{50} \approx 100$ μM), making them more suitable for PDT. In HeLa cells, all complexes showed low micromolar IC_{50} values regardless of light, indicating selective PDT activity of **3** and **4** in A549 cells. Control ligands (Py-BzIm, Tz-BzIm) were inactive, and cisplatin showed antiproliferative activity consistent with published data.[18]

Given their strong PDT performance in A549 cells (PI = 291 for **3**, 1054 for **4**) and the chemotherapeutic potential of **1** and **2**, further biological analyses were conducted on representative complexes from each family. Log *P* measurements revealed slightly higher lipophilicity for **1** and **2**, which could influence uptake. However, ICP-MS analysis showed similar cellular accumulation of **1** and **3** (200.9 ± 56 and 186.3 ± 37 (ng mL^{-1})/10^6 cells), suggesting that differences in their antitumor activity are not solely due to uptake (Fig. S51a).

Cell death mechanism was assessed by Annexin V and PI staining and flow cytometry, and dose-dependent apoptosis was confirmed under light exposure (Fig. 3a and b). Complex **3** triggered significant cell death even at low doses (~90% at 2 × IC_{50}; Fig. 3b-left). In contrast, complex **1** toxicity was moderate at this range (~30% cell death at 2 × IC_{50}) and was enhanced with increasing dose (~70% cell death at 4 × IC_{50}).

Under dark conditions, only complex **1** was evaluated, as complex **3** exhibited a high IC_{50} value (99 ± 1.3 μM). Complex **1** showed a modest cytotoxic effect even at the highest concentration tested (~30% cell death at 13.7 × IC_{50} Fig. 3b-right), suggesting a distinct mechanism of action in the dark and upon irradiation (Fig. S51b). Moreover, cell cycle analysis showed that complex **1** inhibited cell proliferation under both dark and irradiated conditions, producing only minor alterations in the G0/G1 and G2/M phases. These results suggest a cytostatic effect at low doses in both cases (Fig. 3c and Fig. S51c and d). However, complex **3** (IC_{50}) induced G0/G1 arrest in the dark (Fig. S51c). Furthermore, complex **1** and **3** induced dose-dependent intracellular ROS generation in the dark and under irradiation respectively (Fig. S51e) consistent with previous reports on similar Ir(III) complexes.[20] These results suggest that both complexes induce light-triggered apoptosis, particularly potent in the case of complex **3**. In fact, complex **1** at concentrations close to the IC_{50} would exert a cytostatic effect after irradiation, and this effect also predominates in darkness. Subcellular localization is known to play a critical role in the therapeutic efficacy and selectivity of metallodrugs. To better

Table 1 Photophysical data of **1–4** measured in DMSO and/or CH_3CN solution at 298 K

	λ_{em}/nm (λ_{exc}/nm)^a	λ_{em}/nm (λ_{exc}/nm)^b	τ^a/μs	τ^b/μs (τ^d/μs)	$\Phi_{em}{}^a$ ($\Phi_{em}{}^c$)	Φ_Δ ($^1O_2$)^b
1	597, 649, 706 (480)	592, 642, 703 (475)	1.71	0.19 (4.52)	0.02 (0.38)	0.44
2	597, 649, 706 (475)	590, 642, 700 (450)	3.47	0.20 (4.92)	0.02 (0.38)	0.44
3	552, 587, 637 (470)	530, 572, 617 (425)	1.86	0.27	0.16 (0.83)	0.55
4	555, 590, 640 (470)	541, 567 (425)	0.89	0.23	0.15 (0.82)	0.50

Note: Emission (λ_{em}), lifetimes of excited state (τ), emission quantum yields (Φ) and $^1O_2$ generation quantum yield ($^1O_2$, Ø) of compounds **1–4** in (2×10^{-5} M) in DMSO or CH_3CN solutions at 298 K. ^{a} Aerated DMSO solution. ^{b} Aerated CH_3CN solution. ^{c} N_2 saturated DMSO solution. ^{d} N_2 saturated CH_3CN solution.

Open Access Article. Published on 05 novembris 2025. Downloaded on 10.01.2026 17:50:41.
This article is licensed under a Creative Commons Attribution-NonCommercial 3.0 Unported Licence.

Table 2 IC_{50} values (μM) of compounds **1–4**, Py-BzIm, Tz-BzIm and cisplatin incubated with A549 and HeLa. Log *P* values of complexes **1–4**

	A549 IC_{50}(DARK) (IC_{50}(Irr.))	A549 PI	HeLa IC_{50}(DARK) (IC_{50}(Irr.))	HeLa PI	Log *P*
1[a]	0.99 ± 0.24 (0.015 ± 0.002)	66	1.76 ± 1.01 (0.010 ± 0.005)	176	1.59
2[a]	0.65 ± 0.12 (0.017 ± 0.003)	38	0.70 ± 0.60 (0.010 ± 0.003)	70	2.49
3[a]	99 ± 1.30 (0.34 ± 0.02)	291	>5 (0.030 ± 0.022)	—	1.47
4[a]	116 ± 1.10 (0.11 ± 0.02)	1054	1.50 ± 0.70 (0.010 ± 0.001)	150	1.63
Py-BzIm[b]	>100 (n.d.)	—	68.50 ± 0.90 (n.d.)	—	n.d.
Tz-BzIm[b]	>100 (n.d.)	—	>100 (n.d.)	—	n.d.
Cisplatin[b]	9.39 ± 0.08 (n.d.)		8.05 ± 0.13 (n.d.)	—	n.d.

[a] Conditions: 48 h incubation in the dark and under irradiation (470 nm, 10 min, 1.6 J cm^{-2}). PI = IC_{50}(dark)/IC_{50}(light). [b] Conditions: 48 h incubation in the dark only, as these compounds are not light-activatable. Log *P* values from the shake-flask method.[19] n.d.: not determined.

understand the differing therapeutic outcomes of the two Ir(III) families, the intracellular distribution of complexes **1–4** was examined in A549 cells using confocal microscopy. Mitochondria were stained with MitoTracker Deep Red (MTDR). All complexes were internalized by the cells and did not accumulate in the nucleus. Notably, complexes **1** and **2** predominantly localized to mitochondria, as indicated by strong colocalization with MTDR (Pearson coefficients: 0.78 and 0.62, respectively). This mitochondrial accumulation likely contributes to their higher antiproliferative activity in the dark, given the central role of mitochondria in cellular function. In contrast, complexes **3** and **4** showed poor mitochondrial localization (Pearson coefficients <0.35), which may explain their reduced dark activity (Fig. 4 and Fig. S52). These observations are consistent with the organelle's pivotal role in energy production and survival of cells[21] and with prior studies reporting enhanced biological activity in iridium complexes engineered for mitochondrial targeting.[13]

To further confirm the higher mitochondrial accumulation of the benzothiophene-based complex (**1**) compared to its benzothiazole counterpart (**3**), mitochondrial Ir content was quantified by ICP-MS, Fig. S53. Complex **1** showed greater uptake (5.52 ng/10^6 cells) than complex **3** (3.65 ng/10^6 cells), likely due to its higher log *P* value. This aligns with the negatively charged mitochondrial membrane favoring the accumulation of lipophilic, cationic species like complex **1**.[21]

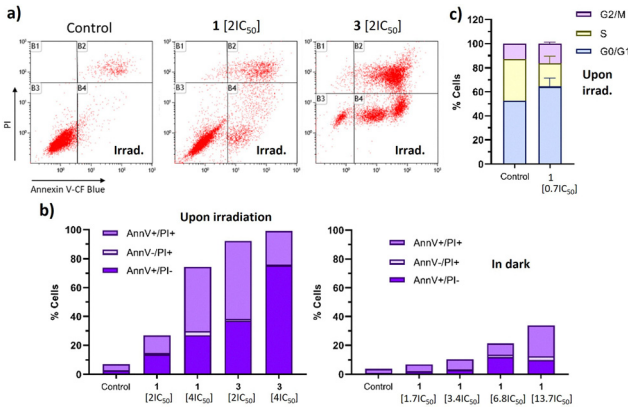

Fig. 3 (a) Dot plots showing A549 cell death after 48 h incubation with **1** and **3**, followed by 470 nm irradiation (10 min, 1.6 J cm^{-2}) using Annexin V-CF Blue/PI staining. (b) Cell death induced by **1** and **3** under light and dark conditions. (c) Cell cycle distribution for compound **1** at the indicated dose post-irradiation.

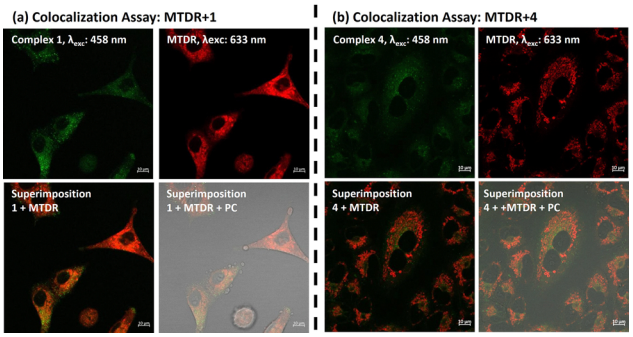

Fig. 4 (a) Confocal images of A549 cells incubated with complex **1** (6 μM, 2 h), then stained with MitoTracker Deep Red (MTDR, 100 nM, 30 min). (b) Same for complex **4**. Excitation: 458 nm (**1** and **4**), 633 nm (MTDR). Emission: 552–623 nm (**1** and **4**), 638–755 nm (MTDR). PC: phase contrast.

To investigate possible lysosomal localization, additional colocalization assays were performed using LysoTracker Deep Red (LTDR). While LTDR showed strong fluorescence in control conditions, its signal disappeared when co-incubated with any of the Ir complexes (Fig. S54), suggesting fluorescence quenching, likely due to singlet oxygen generated upon light activation. This is in line with previous studies reporting singlet oxygen–mediated quenching of fluorescent dyes such as LysoTracker by Danglot and Collot.[22] To determine if this quenching was specific to LTDR, LysoTracker Green (LTG) and LysoTracker Red (LTR) were also tested. Both dyes displayed fluorescence in control cells but were quenched in the presence of the Ir complexes, supporting lysosomal localization and the potential involvement of singlet oxygen in dye quenching (Fig. S55). However, cell-free fluorescence studies under controlled conditions failed to reproduce the quenching effect, suggesting that it may be specific to the cellular environment.

Overall, the colocalization assays indicate that complexes **1–4** localize to both mitochondria and lysosomes. Complexes **1** and **2**, which bear benzothiophene ligands, exhibit greater mitochondrial accumulation than their benzothiazole analogues (complexes **3** and **4**), a feature that may underlie their higher antiproliferative activity under dark conditions. At first glance, this seems counterintuitive, since mitochondrial dysfunction is typically associated with apoptosis,[21] yet complexes **3** and **4**, which show lower mitochondrial accumulation, are the ones inducing apoptotic cell death.

Open Access Article. Published on 05 novembris 2025. Downloaded on 10.01.2026 17:50:41.
This article is licensed under a Creative Commons Attribution-NonCommercial 3.0 Unported Licence.

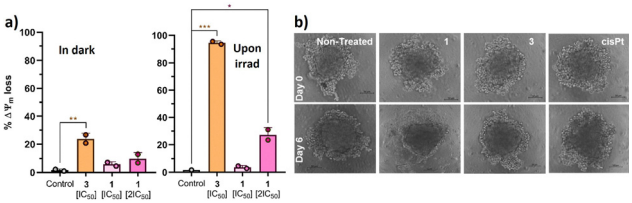

Fig. 5 (a) Percentage of A549 cells with disrupted mitochondrial membrane potential after treatment with complexes **1** and **3**, in the dark and post-irradiation (470 nm, 10 min, 1.6 J cm^{-2}). $*p < 0.05$; $**p < 0.01$; $***p < 0.001$. (b) Morphology and viability of A549 spheroids after 6 days of treatment with complexes **1** and **3** at their IC_{50} values (dark conditions). Scale bar: 50 μm.

To resolve this apparent discrepancy, mitochondrial membrane potential (MMP) was assessed by flow cytometry. As shown in Fig. 5a, complex **3** caused a pronounced loss of MMP following irradiation, consistent with mitochondrial damage and apoptosis.

In contrast, complex **1** had minimal impact on MMP, both in the dark and under irradiation, with only a slight decrease observed at higher doses. These findings support the previously observed cytostatic profile of complex **1** under both conditions, while highlighting the photoactivated cytotoxic nature of complex **3**, driven by significant mitochondrial impairment. Finally, 3D multicellular tumor spheroids (MCTSs) were used to mimic *in vivo* tumor conditions. Treatment of A549 MCTSs with complex **1** led to significant inhibition of growth after six days, outperforming both complex **3** and cisplatin, Fig. 5b and Fig. S56, S57. This supports the higher antitumor activity in dark of complex **1** in both 2D and 3D models and underscores its promise for chemotherapeutic therapy *via* a cytostatic pathway.

This study presents two families of cyclometallated Ir(III) complexes with distinct therapeutic profiles governed by ligand structure. Benzothiophene-based complexes (**1** and **2**) showed potent antiproliferative activity in the dark, consistent with a cytostatic mechanism and mitochondrial accumulation, making them promising chemotherapeutic agents. However, at high concentrations, an apoptotic cell death pattern is observed specially under irradiation. In contrast, benzothiazole-based complexes (**3** and **4**) exhibited strong photocytotoxicity and induced apoptosis upon light activation even at low concentrations, correlating with mitochondrial dysfunction and singlet oxygen generation, positioning them as effective photosensitizers for PDT. Notably, complexes **3** and **4** displayed marked cell-line selectivity, showing higher PDT activity in A549 than in HeLa cells, indicating a differential therapeutic response depending on the cancer type. Subcellular localization, cell death mechanism, and activity in 3D spheroids further support ligand-driven selectivity. These findings highlight the potential of rational ligand design in tuning the mode of action and selectivity of metal-based anticancer agents.

This work was supported by projects PID2022-137862NB-I00, PID2022-136861NB-I00, and PID2022-139296NB-I00, funded by MICIU/AEI/10.13039/501100011033 and the European Union; CNS2023-143600 (MICIU/AEI and NextGenerationEU/PRTR); and COST Action CA22131, LUCES. Financial support from the Gobierno de Aragón–Fondo Social Europeo (E07_23R) and the Spanish network OASIS (RED2022-134074-T) is also acknowledged. M. R. gratefully acknowledges the Fondation pour la Recherche Médicale (FRM, SPF202309017545).

Conflicts of interest

There are no conflicts of interest to declare.

Data availability

Data supporting this article have been included in the supplementary information (SI). Supplementary information: Synthetic procedures, characterisation data, methodology, supporting figures and tables. See DOI: **https://doi.org/10.1039/d5cc04768d**.

CCDC 2405786 (**3**) contains the supplementary crystallographic data for this paper.[23]

Notes and references

1 K. D. Mjos and C. Orvig, *Chem. Rev.*, 2014, **114**, 4540–4563.
2 S. Monro, K. L. Colón, H. Yin, J. Roque, P. Konda, S. Gujar, R. P. Thummel, L. Lilge, C. G. Cameron and S. A. McFarland, *Chem. Rev.*, 2019, **119**, 797–828.
3 Y. Wu, S. Li, Y. Chen, W. He and Z. Guo, *Chem. Sci.*, 2022, **13**, 5085–5106.
4 B. Kar, U. Das, N. Roy and P. Paira, *Coord. Chem. Rev.*, 2023, **474**, 214860.
5 J. Sanz-Villafruela, A. Carbayo, M. Martínez-Alonso and G. Espino, *Coord. Chem. Rev.*, 2025, **534**, 216572.
6 M. Negi, T. Dixit and V. Venkatesh, *Inorg. Chem.*, 2023, **62**, 20080–20095.
7 T. Feng, Z. Tang, J. Karges, J. Shu, K. Xiong, C. Jin, Y. Chen, G. Gasser, L. Ji and H. Chao, *Chem. Sci.*, 2024, **15**, 6752–6762.
8 J. Kasparkova, V. Novohradsky, J. Ruiz and V. Brabec, *Chem.-Biol. Interact.*, 2024, **392**, 110921.
9 F.-X. Wang, M.-H. Chen, Y.-N. Lin, H. Zhang, C.-P. Tan, L.-N. Ji and Z.-W. Mao, *ACS Appl. Mater. Interfaces*, 2017, **9**, 42471–42481.
10 J. Sanz-Villafruela, C. Bermejo-Casadesús, G. Riesco-Llach, M. Iglesias, M. Martínez-Alonso, M. Planas, L. Feliu, G. Espino and A. Massaguer, *Inorg. Chem.*, 2024, **63**, 19140–19155.
11 K. E. De Visser and J. A. Joyce, *Cancer Cell*, 2023, **41**, 374–403.
12 M. Redrado, E. Romanos, A. Benedi, G. Canudo-Barreras, I. Marzo, M. C. Gimeno and V. Fernández-Moreira, *Inorg. Chem. Front.*, 2024, **11**, 1828–1838.
13 L. Wang, J. Karges, F. Wei, L. Xie, Z. Chen, G. Gasser, L. Ji and H. Chao, *Chem. Sci.*, 2023, **14**, 1461–1471.
14 T. Yoshihara, Y. Yamaguchi, M. Hosaka, T. Takeuchi and S. Tobita, *Angew. Chem., Int. Ed.*, 2012, **51**, 4148–4151.
15 S. Ladouceur, D. Fortin and E. Zysman-Colman, *Inorg. Chem.*, 2011, **50**, 11514–11526.
16 T. Yoshihara, S. Murayama, T. Masuda, T. Kikuchi, K. Yoshida, M. Hosaka and S. Tobita, *J. Photochem. Photobiol., A*, 2015, **299**, 172–182.
17 A. I. Solomatina, K. M. Kuznetsov, V. V. Gurzhiy, V. V. Pavlovskiy, V. V. Porsev, R. A. Evarestov and S. P. Tunik, *Dalton Trans.*, 2020, **49**, 6751–6763.
18 D.-H. Cai, C.-L. Zhang, Q.-Y. Liu, L. He, Y.-J. Liu, Y.-H. Xiong and X.-Y. Le, *Eur. J. Med. Chem.*, 2021, **213**, 113182.
19 S. Amézqueta, X. Subirats, E. Fuguet, M. Rosés and C. Ràfols, *Liquid-Phase Extraction*, Elsevier, 2020, pp. 183–208.
20 M. Redrado, A. Benedi, I. Marzo, A. L. García-Otín, V. Fernández-Moreira and M. C. Gimeno, *Chem. – Eur. J.*, 2021, **27**, 9885–9897.
21 S. Fulda, L. Galluzzi and G. Kroemer, *Nat. Rev. Drug. Discovery*, 2010, **9**, 447–464.
22 L. Saladin, V. Breton, V. Le Berruyer, P. Nazac, T. Lequeu, P. Didier, L. Danglot and M. Collot, *J. Am. Chem. Soc.*, 2024, **146**, 17456–17473.
23 CCDC 2405786: Experimental Crystal Structure Determination, 2025, DOI: **10.5517/ccdc.csd.cc2lrf0t**.

 This journal is © The Royal Society of Chemistry 2025